Phase field modeling of partial remelting during reheating of a multiphase peritectic solidification microstructure

A. Viardin, G. Boussinot, Julien Zollinger

▶ **To cite this version:**

A. Viardin, G. Boussinot, Julien Zollinger. Phase field modeling of partial remelting during reheating of a multiphase peritectic solidification microstructure. Materialia, 2022, 26, pp.101590. 10.1016/j.mtla.2022.101590 . hal-03798198

HAL Id: hal-03798198

https://hal.univ-lorraine.fr/hal-03798198

Submitted on 5 Oct 2022

HAL is a multi-disciplinary open access archive for the deposit and dissemination of scientific research documents, whether they are published or not. The documents may come from teaching and research institutions in France or abroad, or from public or private research centers.

L'archive ouverte pluridisciplinaire **HAL**, est destinée au dépôt et à la diffusion de documents scientifiques de niveau recherche, publiés ou non, émanant des établissements d'enseignement et de recherche français ou étrangers, des laboratoires publics ou privés.

Phase field modeling of partial remelting during reheating of a multiphase peritectic solidification microstructure

A. Viardin[a], G. Boussinot[a,*], J. Zollinger[b]

[a] *ACCESS e.V., Intzestrasse 5, D-52072 Aachen, Germany.*
[b] *Institut Jean Lamour, Université de Lorraine/CNRS, ARTEM Campus, F-54011 Nancy, France.*

Abstract

While they are known for years to be the main source of equiaxed grains in metallurgical processes such as casting, melting and remelting phenomena currently receive an increasing attention owing to the developments of additive manufacturing. In multiphase alloys, *i.e.* having a eutectic or peritectic microstructure, these phenomena still remain poorly documented. In this work, the solidification and subsequent remelting of peritectic alloys have been studied using phase field simulations, with emphasis on the influence of the peritectic equilibrium, that yields the peritectic reaction $L+\beta \rightarrow \alpha$ below the peritectic temperature and the reverse peritectic reaction $\alpha \rightarrow L+\beta$ above. During solidification, the growth of the peritectic α phase has little influence on the growth of the pro-peritectic β phase. On the other hand, the evolution during remelting of a previously solidified peritectic microstructure is more complex and involves temperature gradient zone melting and liquid film migration phenomena. Close to the peritectic temperature, the reverse peritectic reaction is driven by liquid film migration, and some scenarii are evidenced depending on whether the growth takes place without triple junction from a pure α phase or with a triple junction along the α/β interface. At the scale of the mushy zone, the Temperature Gradient Zone Melting phenomenon also occurs but remains incomplete at the time scale investigated here. Finally, a new mechanism for fragmentation, induced by the reverse peritectic reaction during remelting, has been identified.

1. Introduction

Among the common univariant reactions, peritectic systems have received much less attention than eutectics, despite the presence of a peritectic reaction in many alloy systems of technological interest such as steels, brass and titanium alloys among many others. A peritectic equilibrium is characterized by the reaction $Liq. + \beta \rightarrow \alpha$ upon cooling, where β and α are two distinct solid phases. The solidification of alloys having a peritectic plateau is relatively well documented [1]. Under typical processing conditions, the growth is characterized by (i) a triple junction (TJ) where the three phases are in equilibrium and the so-called peritectic reaction takes place [39]; (ii) the peritectic transformation where the peritectic phase α grows at the expense of the properitectic phase β, the latter being a solid state transformation [2]. In peculiar solidification conditions, such as low solidification velocities, some more remarkable microstructures can emerge, such as banded structure or coupled growth [3, 4]. The mechanism of formation of the aforementioned peritectic solidification microstructures are fairly well known and quantitatively modeled, in particular with the phase field method [5–7, 40].

Melting received much less attention than its reverse transformation, *i.e.* solidification, particularly for multiphase microstructures. From the viewpoint of thermodynamics, it is obviously the reverse of solidification. However, the dynamic behaviors of melting and solidification of alloys are far from being symmetrical [8]. In many solidification processes, a local remelting phenomenon, i.e. an increase of liquid fraction at the microstructure scale can occur [9]. In the recently developed additive processes, the melting of a previously solidified microstructure occurs at each layer deposition stage and can have consequences on further solidifying steps [10]. Except for the latter case where remelting is induced by a heat source, other phenomena can induce remelting. Two different *scenarii* are shown in Figure 1 for a binary alloy of composition C_0 having a partition coefficient $k < 1$ and assuming the lever rule applies at the scale of the mushy zone. Case *a* corresponds to the case where fluid flow feeds the mush with liquid coming from hotter regions, leading to a local increase of temperature and thus an increase of liquid fraction. Case *b* corresponds to the case of liquid flowing from the mush to the dendrite tips, thus enriching the local composition with interdendritic liquid. The latter case is one of the cause of freckle formation. In single phase binary alloys, remelting has received attention as it can be a cause of dendrite fragmentation, which is the main source of equiaxed grains in castings [11]. The solid/liquid interface curvature also contributes to fragmentation: the secondary dendrite arms have a large curvature at the junc-

*Corresponding author

tion with the primary arms, decreasing the local melting point through the Gibbs-Thomson effect. A complex three dimensional interaction between the principal curvatures of the solid/liquid interface leads to necking and then fragmentation [12]. A uniform temperature increase can thus provoke dendrite fragmentation [13], but can lead to other phenomena. Salloum-Jaoude *et al.* have shown that interrupted directional growth of a dendritic structure could produce a Temperature Gradient Zone Melting (TGZM) [14], as described by Tiller [15] and modeled by Boussinot *et al.* [16]. The only studies on melting of peritectics were done numerically on a TJ isothermally held at a temperature above the peritectic plateau [17, 18]. In this case, a liquid film migration (LFM) phenomenon takes place. It corresponds to a combined motion of a melting and a solidification fronts, coupled through the diffusion field in the liquid.

This work addresses the two-dimensional simulation of the remelting of a peritectic microstructure corresponding to case *a* in Fig. 1. The evolution during remelting of a multiphase peritectic microstructure and of its TJ has, to the knowledge of the authors, only scarcely been investigated. In particular experimentally, in the case of Fe-C alloy, the reverse peritectic reaction was recently associated with fragmentation of primary phase dendrite arms [41]. Here, the Ti-Al system has been chosen, since it is of technological interest and requires processes inducing important fluid flows, such as centrifugal casting [19]. While the remelting of a peritectic microstructure could have a positive impact on dendrite fragmentation [20], the precise mechanism from which it originates is still vague [41]. The amount of fragments seems related to the fraction of properitectic phase, but it is unclear whether it is a consequence of the solidification process or due to a melting or remelting phenomenon [21]. In order to discriminate these effect, a first part will be devoted to study the influence of temperature difference between the solidification front and the peritectic front (*via* the composition of the alloy) on the morphological and undercooling evolution of an isolated dendrite. Secondly, the microstructure evolution of a Ti-48 at.%Al, a composition which is representative of most alloys of technological interest, during a partial remelting induced by a uniform reheating of the mushy zone will be addressed. Through our 2D simulations, which are not describing the above mentioned complex 3D effect of curvature on necking, it will be shown that several phenomena, such as TGZM and LFM, drive the microstructure evolution during remelting, eventually producing fragments through a new mechanism involving the reverse peritectic reaction.

2. Model and simulation description

2.1. Phase-field model

Two-dimensional simulations were performed, based on the multiphase field model linked to thermodynamic databases [22, 23] as implemented in the phase field software MICRESS [24]. A finite-difference correction was used to improve the accuracy of the results [25]. Furthermore, an anti-trapping current and mobility correction according to the thin interface limit are considered [26]. This phase field model has already been used to study the evolution of a mushy zone in Al-alloys in more detail [27, 28].

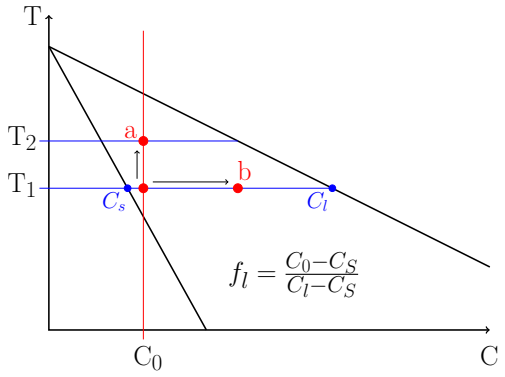

Figure 1: Schematic representation of transformation paths leading to local remelting in an idealised binary phase diagram. See text for details.

2.2. Alloy data

TiAl alloys with concentrations varying between 47.5 and 48.6 % were selected for this study. In Figure 2(a) and (b), the TiAl phase diagram and a zoom in the area of interest around the peritectic equilibrium are shown. In Figure (b), the liquidus and solidus slopes for both phases, as well as the β/α and α/β slopes were linearised for the simulations. The corresponding parameters, together with the thermophysical properties and nucleation data are given in Table 1. As will been seen in the next sections, most of the microstructure evolution is driven by the diffusion in the liquid phase. With this regards, some simplifying assumptions were made, *i.e.* the diffusion coefficient in the solid phases were given the same value and the interfacial enery between all solid phases and the liquid, *i.e.* $\sigma_{\beta l}$, $\sigma_{\alpha l}$ and $\sigma_{\beta\alpha}$ are equal. Anisotropy has only been introduced for the l/β interface in order to obtain a realistic primary dendritic structure.

2.3. Solidification simulation parameters

The simulations are performed in a rectangular domain of 0.5 mm×2.25 mm, the simulated time interval is 500 s. The simulations starts from explicitly set β nuclei at the middle-bottom of the calculation domain. According to the orders of magnitude separating the heat and chemical diffusion coefficient, we assume a unidirectional and constant temperature gradient $G_T = 120\text{K/cm}$ aligned with the z direction, so that the time dependent temperature field $T(z,t)$ is :

$$T(z,t) = T_b(t) + G_T z \tag{1}$$

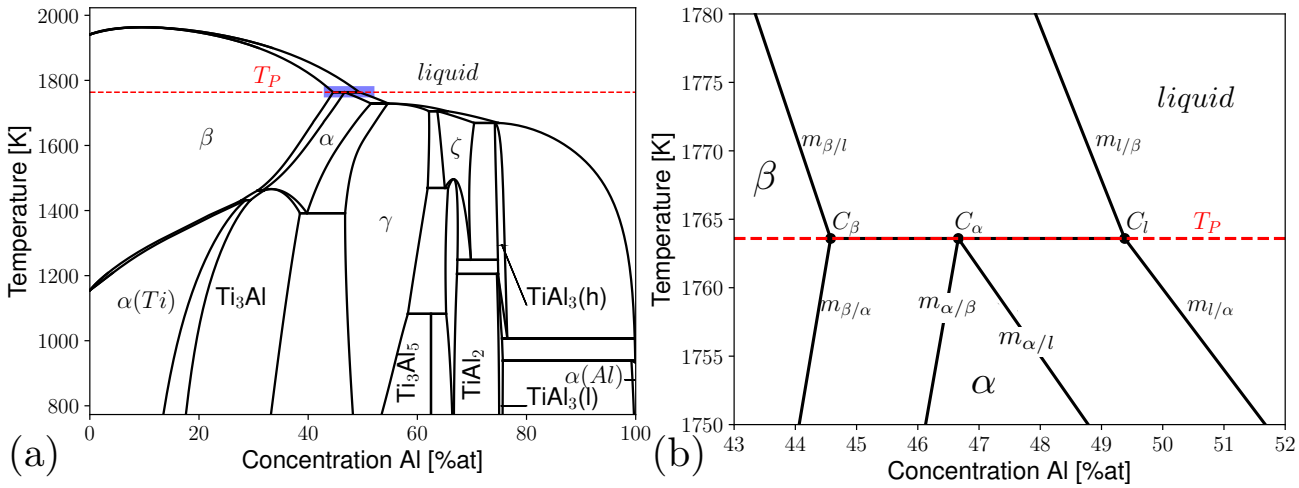

Figure 2: Left : TiAl phase diagram determined by [29], right : zoom on the peritectic zone in blue rectangle on the left figure.

Table 1: Thermodynamic data, thermophysical properties and nucleation parameter used in the present calculations.

T_p	Peritectic temperature	1763.6	K	[29]
$m_{l/\beta}$	Liquidus slope l/β	-11.26	K/at.%	[29]
$m_{\beta/l}$	Solidus slope β/l	-13.33	K/at.%	[29]
$\Delta S_{l/\beta}$	Entropy of fusion l/β	0.62	J/(cm^{3}K)	[29]
$m_{l/\alpha}$	Liquidus slope l/α	-5.92	K/at.%	[29]
$m_{\alpha/l}$	Solidus slope α/l	-6.40	K/at.%	[29]
$\Delta S_{l/\alpha}$	Entropy of fusion l/α	0.76	J/(cm^{3}K)	[29]
$m_{\beta/\alpha}$	Liquidus slope β/α	26.45	K/at.%	[29]
$m_{\alpha/\beta}$	Solidus slope α/β	25.41	K/at.%	[29]
$\Delta S_{\alpha/\beta}$	Entropy of transformation α/β	0.14	J/(cm^{3}K)	[29]
C_β	Peritectic concentration β	44.6	at.%	[29]
C_α	Peritectic concentration α	46.7	at.%	[29]
C_l	Peritectic concentration liquid	49.4	at.%	[29]
$\sigma_{\varphi l}$	Solid/liquid interfacial energy ($\varphi = \alpha, \beta$)	0.1	J/m^2	[30]
ϵ_β	Interfacial energy anisotropy in β	1.1%	/	[30]
D_l	Diffusion coefficient in the liquid	$3 \cdot 10^{-9}$	m^2/s	[31]
D_β	Diffusion coefficient in β	$3 \cdot 10^{-11}$	m^2/s	P.W.
D_α	Diffusion coefficient in α	$3 \cdot 10^{-11}$	m^2/s	P.W.
ΔT_{nuc}	Nucleation undercooling of α	2	K	P.W.

where $T_b(t)$ is the temperature at the bottom of the simulation (z=0) and z is the distance to the bottom of the simulation domain. During solidification, we use a frozen-temperature approximation [38] with a constant imposed cooling rate, i.e. $\dot{T}_b(t)$=-0.3 K/s, corresponding to a pulling velocity of 25 μm/s.

The α phase is nucleated at the liquid/β (l/β in the following) interface along the dendrite arm. The α nuclei are described by a nucleation undercooling ΔT_{nuc} of 2 K and a minimum distance between nucleation sites. A new nucleus is activated whenever the local undercooling, which is determined as function of the local temperature, the concentration and the curvature of the l/β interface exceed the specified critical value. Nucleation of α occurs quickly at the beginning of the solidification, and rapidly the system evolves toward steady state. The computational domain moves with the solid/liquid interface in order to maintain a constant distance of 700 μm between the most advanced point of the interface and and the top boundary. The global concentration C_0 of the alloy is varied, and the temperature at the bottom of the simulation box is set to provide a constant departure from the concentration-dependent liquidus temperature $T_l(C_0)$.

2.4. Remelting simulation parameters

For these calculations a Ti-48% Al is considered. As explained later on, we increase the width of the simulation box to 1 mm in order for secondary arms of the primary β dendrite to be well-developed. At the end of solidification stage when t=0, the thermal gradient is kept constant (G_T=120 K/cm) and an increase in temperature ΔT, homogeneous in space, is imposed to the system, i.e.

$$T(z,t) = T_b(t) + G_T z + \Delta T \tag{2}$$

We performed two types of simulation. In the first one, we used $\dot{T}_b(t) = 0$, i.e. $T_b(t) = T_b(0)$. While the dendrite tip is at T_{tip} during solidification, it is brought to

$T_{tip} + \Delta T$ and no further cooling rate is applied. This leads to a reheating and a holding stage during which the microstructure evolves. Simulations were performed with $\Delta T = 6$K, 8K, 10K and 12K. In the second one, the latent heat release or absorption due to a change in the fraction of solid phase was accounted for, i.e. $(c_p/L)\dot{T}_b(t) = -(1/v)\int_v \dot{\phi}_l dv$, where c_p is the heat capacity, L is the latent heat, v is the volume of the simulation box and ϕ_l is the phase field representing the liquid phase. Here, rapidly, all ΔT yield the same temperature field, owing to a damping linked to the fact that the larger ΔT is, the larger the absorbed latent heat due to melting is. As a consequence, in the following, only one case of simulation with latent heat (LH) will be shown.

3. Solidification microstructures

In this section, (i) the influence of peritectic reaction on the growth of β dendrite, and (ii) the influence of the properitectic β phase on the driving force at the TJ, are investigated. Figure 3 shows concentration maps at steady-state, after 500s of simulated time, for concentration ranging from 47.5% to 48.6%. The microstructures are typical of what is usually observed in peritectic solidifying systems. The primary β dendrites grows steadily and, after nucleating, the peritectic α phase grows along the trunk and reaches a steady state illustrated in Figure 3. As can be seen in the figure, when the aluminium concentration increases, the amount of primary β decreases and the secondary dendrite arms have less time to develop. For concentration $>$ 48.4%, no secondary dendrite arms are observed.

The dimensionless undercooling of the β dendrite tip, Δ_{tip}, is given by:

$$\Delta_{tip} = \frac{T_{tip} - T_l(C_0)}{T_s(C_0) - T_l(C_0)}. \quad (3)$$

Here

$$T_l(C_0) = T_p + m_{l/\beta}(C_l - C_0), \quad (4)$$
$$T_\beta(C_0) = T_p + m_{\beta/l}(C_\beta - C_0), \quad (5)$$

where T_{tip} is the temperature at the tip, C_0 is the initial concentration, T_p, $m_{l/\beta}$, C_l, C_β are defined in Figure 2(b) and given in Table 1. The evolution of Δ_{tip} for the investigated composition range is presented in Figure 4. It can be observed that the variation of Δ_{tip} is rather small (around 2% of the total undercooling) suggesting a very weak influence of the diffusion field around the TJ on the dendrite tip. Nevertheless, it should be noted that Δ_{tip} increases between 48.5 and 48.6% Al; due to the cumulated contribution of the solute rejection of both phases. This increase, while noticeable in Figure 4, remains mainly negligible and in the order of 3% for undercooling worth a few K. Indeed, although the distance between the TJ and the tip diminishes when C_0 increases (according to the fact that $T_l(C_0) - T_p$ decreases when C_0 increases), it is still much larger than the characteristic length scale (analog to the lamellar spacing in eutectics [32]) of the diffusion field around the triple junction d_0/Δ_{peri} [33], where d_0 is the capillarity length and Δ_{peri} is the dimensionless driving force at the TJ given by:

$$\Delta_{peri} = \frac{C_{l\alpha}(T_{TJ}) - C_{l\beta}(T_{TJ})}{C_\alpha - C_\beta} \quad (6)$$

where

$$C_{l\alpha}(T_{TJ}) = C_l + \frac{T_p - T_{TJ}}{m_{l/\alpha}}, \quad (7)$$
$$C_{l\beta}(T_{TJ}) = C_l + \frac{T_p - T_{TJ}}{m_{\beta/l}}, \quad (8)$$

with T_{TJ} the temperature of the "hottest" triple junction. On the other hand, the variation of the distance between the TJ and the tip $(T_{TJ} - T_{\rm tip})/G_T$ leads to a strong dependence on C_0 of the side branching activity on the beta dendrite, i.e. the larger is $(T_{TJ} - T_{\rm tip})/G_T$, the longer are the secondary arms. For large enough C_0, no secondary arms develop. This effect has a strong influence on Δ_{peri}, that is attributed to the necessity for the peritectic α phase to grow around the secondary arms. Indeed, while the pulling velocity V_{pull} is the same for all C_0, the distance that has to cover the TJ depends strongly on the length L of the secondary arms. It has been checked that, in 3D calculations (not shown here), the TJ also goes around the secondary arms and does not leave any free beta-liquid interface in its rear at lower temperatures.

When a steady-state is reached, while Δ_{peri} is not strictly constant in time due to the dynamics of the TJ around the secondary arms, one may however extract a time-averaged Δ_{peri}. The latter is linked to the velocity V_{TJ} at which the TJ propagates along the l/β interface, through the scaling law: $d_0 V_{TJ}/D_l \sim \Delta_{peri}^2$ [33]. Equating the time W/V_{pull} needed for the TJ to cover in the growth direction a length of the order of the width W of the secondary arms, and the time needed for the TJ to propagate along the secondary arm L/V_{TJ}, the scaling law

$$\Delta_{peri} \sim \sqrt{\frac{d_0 V_{pull}}{D}\frac{L}{W}} \quad (9)$$

is obtained. Δ_{peri} increases with the ratio L/W, *i.e.* when secondary arms develop, and thus decreases when C_0 increases. This is what can be observed in Figure 5, with Δ_{peri} decreasing by a factor 3, in the investigated composition range. Let us note that the limiting case for which no secondary arms exist ($C_0 \geq 48.5$), is provided by setting $L/W \sim 1$ since in this case $V_{pull} \sim V_{TJ}$. Let us note also that using the capillarity length for the α phase

$$d_\alpha = \frac{\sigma_{SL}}{\Delta S_{l/\alpha}|m_{l/\alpha}|(C_L - C_\alpha)}, \quad (10)$$

for which a value of $d_\alpha \simeq 2.4 \times 10^{-7} m$ is found, leads to $\sqrt{V_{pull} d_\alpha / D_l} \simeq 0.046$, which is consistent with the value

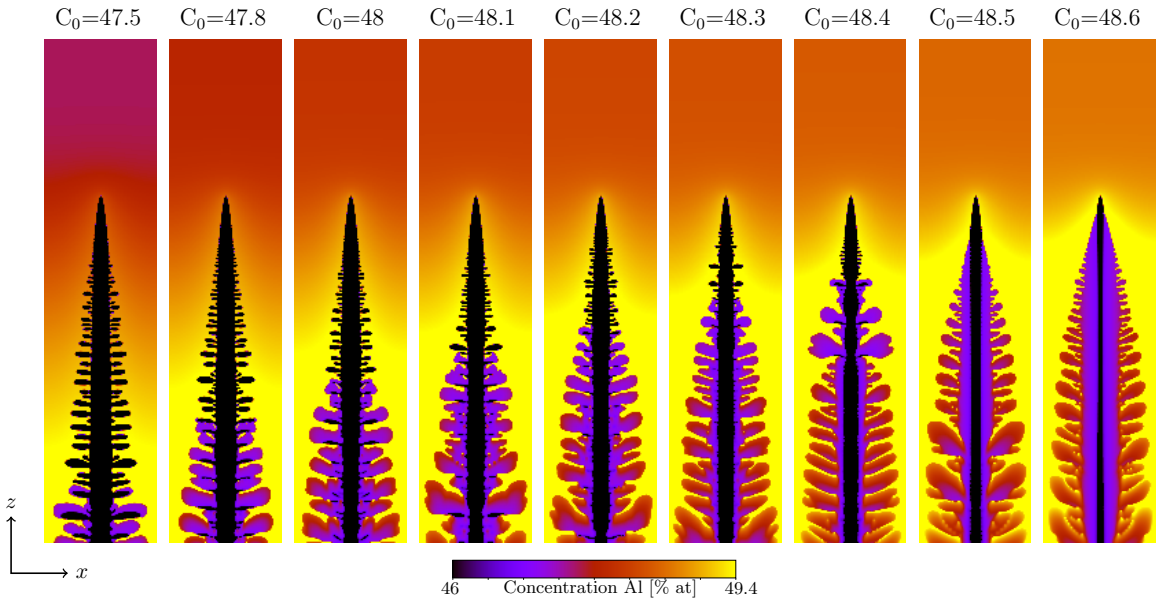

Figure 3: Al-concentration fields at t=500s for initial aluminium concentration ranging from 47.5% to 48.6%at.

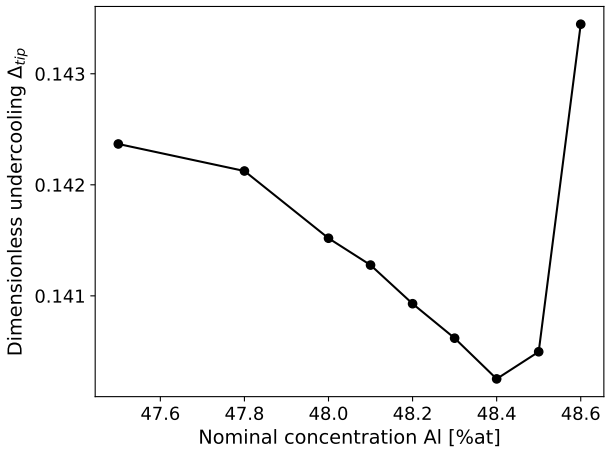

Figure 4: Evolution of the dimensionless dendrite tip Undercooling calculated from Eq. 3 for the composition range investigated.

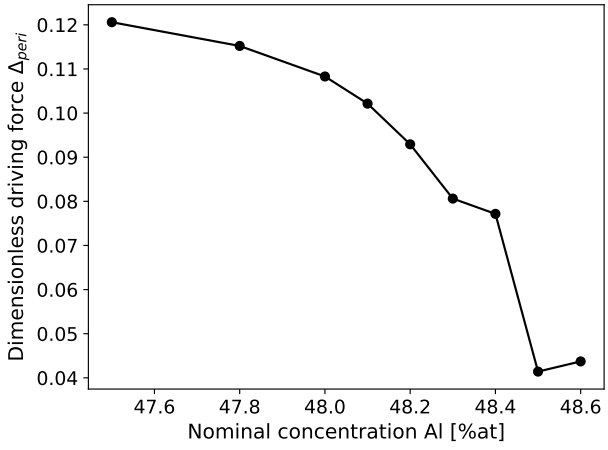

Figure 5: Evolution of the dimensionless driving force at the triple junction calculated with the Eqn. 6 for the composition range investigated.

we obtain for Δ_{peri} when no secondary arm develop, i.e. $\Delta_{peri} \simeq 0.042$.

To summarise the results obtained on solidification, the α phase is found to have only a very weak influence on the tip of the β dendrite, even when the distance between the TJ and the dendrite tip is small enough so that no secondary arms develop. For the investigated composition range, the temperature of the TJ decreases with C_0 because of the development of secondary arms on the primary β dendrite. No fragmentation of secondary dendrite arms induced by the peritectic reaction was observed. With the present simulations, it seems that the peritectic reaction is not the phenomenon inducing dendrite fragmentation. One should note that several 3D simulations were carried out with the same parameters and no fragmentation was found either. Here we were interested in the possibility for the complex structure of the TJ during a purely diffusive peritectic reaction to promote fragmentation. The latter can be however also promoted by heat and solute advection due to fluid flow, which is beyond the scope of this paper. Moreover the peritectic reaction can also be influenced by mechanical interactions due to changes in crystallographic structure. Here we assume that the stresses are relaxed in the presence of the liquid phase and of incoherent solid-solid interfaces.

4. Remelting microstructures

4.1. General observations

A partial remelting stage, as described in section 2.4, is applied to the microstructure inherited from a steady-state solidification of a 48wt% Al alloy in a 1 mm wide simulation box, chosen because it exhibits well-developed secondary dendrite arms. The initial microstructure obtained

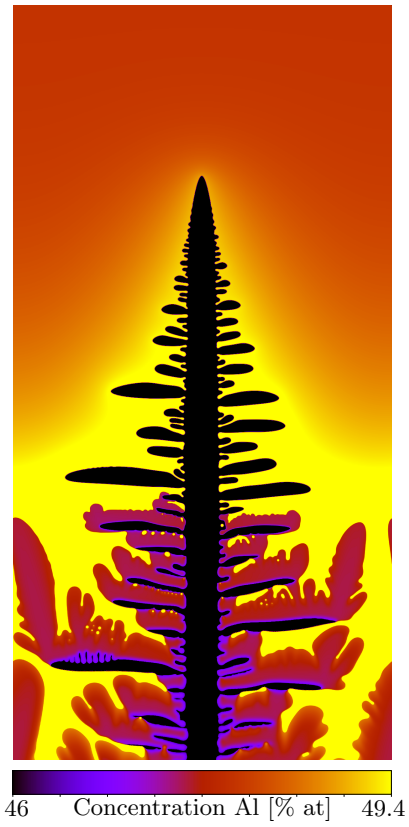

Figure 6: Initial microstructure for our investigation on holding stage

at the end of the solidification stage is presented in Figure 6. From this initial state, a reheating ΔT ranging from 6 to 12 K was applied, without and with accounting for the release of latent heat. An overview of the microstructure evolution with time for those different parameters are presented in Figure 7, in which the red markers indicate the peritectic temperature T_p. A reminder is that, with latent heat, the temperature field becomes rapidly independent of ΔT, and thus only one case is represented in the figure. For the simulations where ΔT was applied without accounting for the latent heat release/absorption, the microstructure evolves in a similar way; the only difference being that it evolves faster when ΔT increases, thus increasing the driving force for remelting. The case with latent heat reveals a different morphological evolution. All these cases will be described and analysed with more details in the following.

Before that, a point has to be addressed. During the reheating and holding stages, the microstructure cannot evolve towards the thermodynamic equilibrium since it is subjected to a thermal gradient. Nevertheless, in absence of coupling between heat fluxes and chemical driving forces (and symmetrically between solute fluxes and thermal driving forces), *i.e.* without the so-called Soret effect, the system evolves towards a stationary state with vanishing solute fluxes. This stationary state is schematically illustrated in Figure 8. At high temperatures the liquid is at the nominal concentration C_0=48% (it is at a slightly different concentration when the liquid is not considered as infinite). A flat β/liquid interface is positioned at the liquidus temperature $T_l(C_0)$, as observed during the holding a mushy zone in a temperature gradient [14]. Then a β/α interface is positioned at a lower temperature (smaller than T_p), such that the concentration is constant across the β layer and equals $C_\beta - (T_p - T_l(C_0))/m_{\beta/l}$, as illustrated in Fig. 8. At lower temperatures, the α phase is present with a concentration $C_\alpha - (C_l - C_0)m_{\beta/\alpha}m_{l/\beta}/(m_{\alpha/\beta}m_{\beta/l})$.

This stationary state with no solute fluxes is very long to establish. It has been shown extensively [14, 16] that the dynamics during a holding stage (without reheating) is first controlled by the TGZM phenomenon [15], during which any solid/liquid interface in the mushy zone migrates towards higher temperatures until it reaches the bulk liquid or until the liquid domain that it delimitates vanishes. While the TGZM process leaves a concentration gradient in the solid, the trunk of the β dendrite, which is not subjected to TGZM in the present case since the dendrite growth direction is aligned with the thermal gradient [34], provides another source of concentration heterogeneity in the solid after completion of the TGZM phenomenon, *i.e.* after the solidification of the mushy zone. For the stationary state described above to be reached, the concentration field thus has to be homogenized through a very slow solid state diffusion, which is out of the scope of this paper. As can be seen in Fig. 7, the present work concerns a much shorter time scale. Concentration gradients in the solid, β dendritic tip and liquid pockets in the mushy zone are still present after 500s of evolution.

Despite the relatively short investigated time scale in comparison to the time needed to reach the stationary state, several observations deserve attention. They are linked to the specificity of the peritectic system under melting conditions. Above T_p, the alloy undergoes partial melting, with the α phase transforming into a $(\beta + L)$ mixture. This is the reverse peritectic reaction, that has been recently associated to a fragmentation-assisted grain refinement [41]. First of all, a qualitative difference is observed between the microstructure after 500s whether or not the latent heat is accounted for (see Fig. 7). The liquid fraction at temperatures immediately above T_p is much larger when latent heat is accounted for than when it is not. This can be understood from the evolution of the temperature in the sample with latent heat, here the temperature at the bottom of the simulation box T_b as shown in Fig. 9, the rest of the temperature field being determined by the thermal gradient. In this figure, it can be observed that T_b is mainly increasing, meaning that accounting for latent heat induces a heating rate over the sample. Therefore there is continuous production of liquid in accordance to the reverse peritectic reaction $\alpha \rightarrow (\beta + L)$. On the opposite, the temperature remains constant without implementing latent heat, and the liquid fraction decreases in time. It is interesting to note that the dark liquid-free part of the mushy zone pointed by a white arrow in Figure 7 in the simulation with latent heat

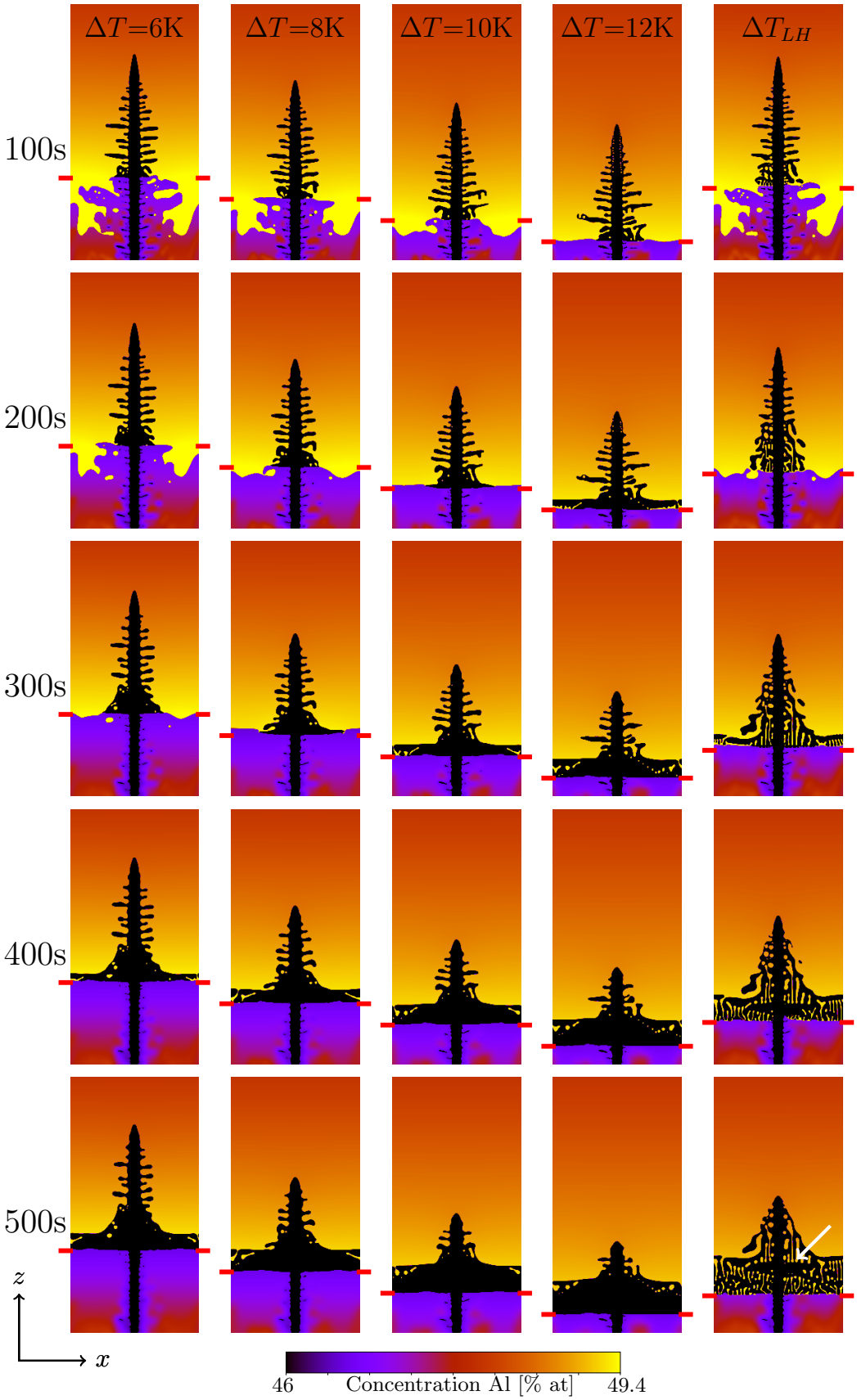

Figure 7: Al-concentration fields at different time steps of holding stage in a temperature gradient (nominal concentration 48%.at) for different temperature at the bottom ($T_b + \Delta T$) and latent heat (LH). Red markers indicate the position of the peritectic temperature (T_p).

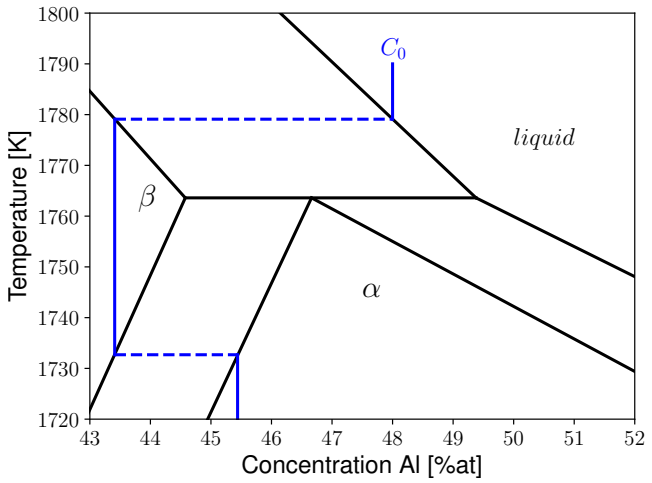

Figure 8: Schematic phase diagram describing the transformation path to reach a stationnary state (in blue). See text for details.

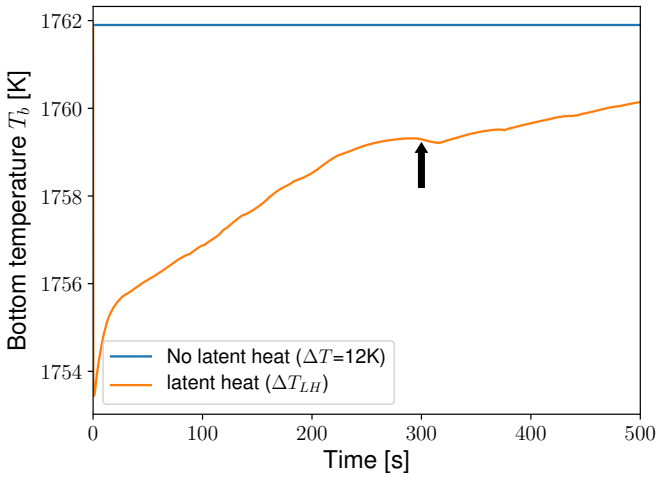

Figure 9: Comparison of temperature at the bottom (T_b) for ΔT_{LH} and ΔT=12 K (see Fig. 7)

corresponds to the solid produced during the interval of time, pointed also by an arrow in Fig. 9, at which T_b saturates and slightly decreases. Between 300 s and 500 s, this solid has undergone a TGZM dynamics.

In Ref. [18], it was shown that the reverse peritectic reaction $\alpha \rightarrow (\beta + L)$, in isothermal conditions above T_p, proceeds through a LFM process. The system takes advantage of the fast diffusion in the liquid film (i.e. the transformation velocity being proportional to the diffusion coefficient in the liquid, rather than to the diffusion coefficient in the solid), driven by $C_{l\alpha} - C_{l\beta}$ the difference in equilibrium concentration of the liquid whether in contact with α or β. The LFM process in a thermal gradient can be related to the existence of a metastable equilibrium for the liquid, sandwiched between the two solid phases, i.e. β at high temperatures and α at low temperatures. As schematically depicted in Figure 10, the two solids inherited from solidification induce a concentration gradient between the liquid/β and the liquid/β interfaces, whose magnitude then depends on the thermal gradient.

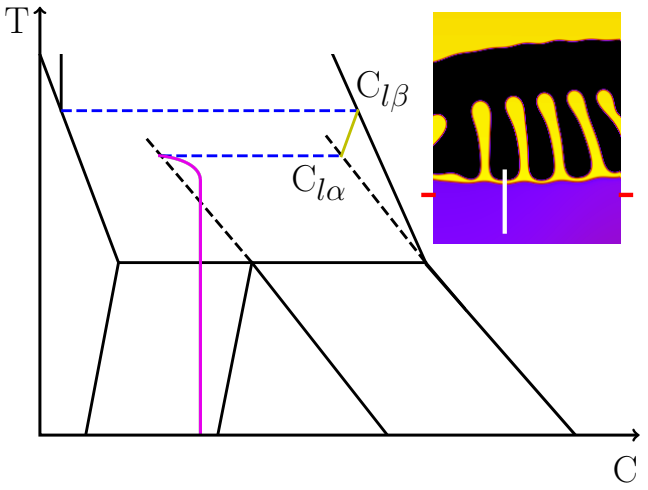

Figure 10: Schematic phase diagram describing the liquid film migration path after reheating the mushy zone and accounting for latent heat. The insert shows a corresponding microstructure (that will be discussed in section 4.2) and the vertical white line along which the concentration profile is plotted.

Small concentration gradients may thus emerge and lead to a close-to-equilibrium pattern formation scenario. In our simulations, there are several illustrations of this phenomenon, that will be pointed out in the next sections.

4.2. Downward tertiary branching and growth

As described in Section 3, the peritectic α phase front grows along the β/liquid interface during solidification, with the TJ at a temperature slightly smaller than T_p. The simulations with re-heating being initialized with the microstructure presented in Fig. 6, it can be seen that a certain amount of α phase has melted within the first 100s in Fig. 7 (see red markers indicating the position of T_p), with this amount being directly proportional to ΔT. Figure 11 shows the microstructure after 27s of evolution for $\Delta T = 10$ K, indicating that the melting stage actually takes place on a much shorter time scale. In particular, tertiary branches have grown downward from β dendrite secondary arms while the α phase was melting. This is coherent with the LFM-driven transformation above T_p that is described above: the melting is partial and the β phase grows together with the liquid phase and at the expense of the α phase.

The downward growth of the tertiary branches results from one of the pattern formation scenario linked to LFM. This scenario is illustrated in Fig. 12 with the simulation accounting for latent heat, for which the microstructure experiences heating and where the $\alpha \rightarrow (\beta + L)$ transformation takes place. In the left panel of Figure 12 presenting the whole microstructure, a new dendrite arm (parallel to secondary dendrite arms) has grown laterally and has developed tertiary arms growing downwards. The lateral growth corresponds to another LFM scenario that will be clarified later on. In the right panels of Figure 12, the evolution of the side arms indicated by the white rectangle in

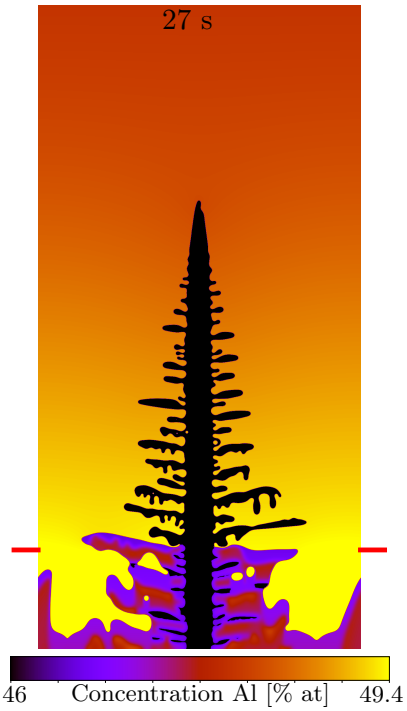

Figure 11: Al-concentration fields at 27 s (ΔT =10K in figure 7). Red markers indicate the position of the peritectic temperature (T_p).

the left panel can be followed for different times. The position of T_p with red markers is also indicated. A downward growth of the side arms with a thin liquid film separating the β and α phases can be seen in the figure. The temperature of the liquid film remains approximately constant, i.e. its distance to T_p is constant, pointing to a steady-state $\alpha \rightarrow (\beta + L)$ transformation. Note that this type of pattern has been evidenced in isothermal conditions (see Fig. 11 in [18]).

This partial melting mode is of primary importance in the simulation with latent heat for which the sample is reheated. This is supported by the tendency of the liquid domains to be strongly elongated along the thermal gradient. However, as soon as the temperature stops to increase (at the arrow in Fig. 9), the liquid film separating β and α vanishes and TGZM drives the liquid pockets upwards in the thermal field, yielding the liquid free zone denoted by an arrow in Fig. 7 and mentioned above. Finally, in view of the evolution of the side arms in Fig. 12, the downward growth of tertiary arms evidenced in Fig. 11 can be understood as the expression of the melting mode described above, during the initial melting of α phase driven by the heating of the microstructure by the amount ΔT.

4.3. Isothermal lateral growth

In this section, two other LFM melting modes will be described. The first one allows the lateral invasion of the microstructure by the β phase slightly above T_p, and takes place with and without accounting for latent heat. In Fig. 13, the case with latent heat for $\Delta T = 10$K is presented, with the whole microstructure in the left panel and a focus on the growing β phase microstructure showed in the white rectangle for different times in the right panels. A needle-like β phase growing at the expense of the α phase can clearly be observed, again with a thin liquid film separating the two solids. Here however, in opposition to the previous case (section 4.2), the migrating liquid film extends along the side of the needle, yielding a dendritic-like front that may be described in terms of two Ivantsov confocal parabolas with the liquid film in between [35].

The second melting mode that has been identified corresponds to the microstructure described theoretically in Brener and Temkin [17] and simulated with the phase field method by Boussinot *et al.* (see Fig. 14 in ref. [18]). It is illustrated in Fig. 15 from the simulation accounting for latent heat. In this figure, the left panel shows the whole microstructure and again the red markers indicate T_p. After 383s, the α/β interface in the white rectangle is overheated above T_p. The evolution of this interface is given in the corresponding right panels. The liquid film grows laterally with a small tip, indicated by white arrows, along the α/β interface. The characteristic size of the tip, i.e. the characteritic length scale at the TJ, is again, as for solidification, of the order of $d_0/|\Delta_{\text{peri}}|$ (Δ_{peri} is negative for melting), here approximately 20 μm. A fundamental difference between solidification and melting should be stressed at this point. Fig. 14 is a close-up around the liquid concentration C_l at the peritectic temperature T_p in the phase diagram. The blue and red dots schematically represent the concentration in the liquid at the triple junction for respectively solidification and melting (below T_p and above). Below (above) T_p the dot lies inside (outside) the $(\alpha + L)$ two-phase region and outside (inside) the $(\beta + L)$ two-phase region. Thus, according to the Gibbs-Thomson effect, the $\alpha - L$ interface is convex (concave) and the $\beta - L$ interface is concave (convex) below (above) T_p. This qualitative difference is illustrated by the corresponding growth pattern below and above T_p.

Finally, far from the laterally propagating liquid tip, downward arms grow similarly as in Figure 13. In Figure 15, it is also interesting to note the untransformed β phase trapped in α phase (see center of the insert at 383 and 392s), that eventually grows. The next paragraph is devoted to this effect.

4.4. Engulfment-assisted fragmentation

Fig. 15 shows the evolution of an untransformed β phase secondary arm (*i.e.* the peritectic transformation was not complete) which was located close to T_p before re-heating the microstructure. In other words, it corresponds to domains of β phase that have been engulfed by the peritectic α phase during solidification. Interestingly, as observed in the left panel of Fig. 16, this β phase domain, which evolution during the early stages of re-heating is presented in the right panels, produces a fragment of β phase during the melting stage. At 35s, the domain of β phase that will lead to the formation of the fragment

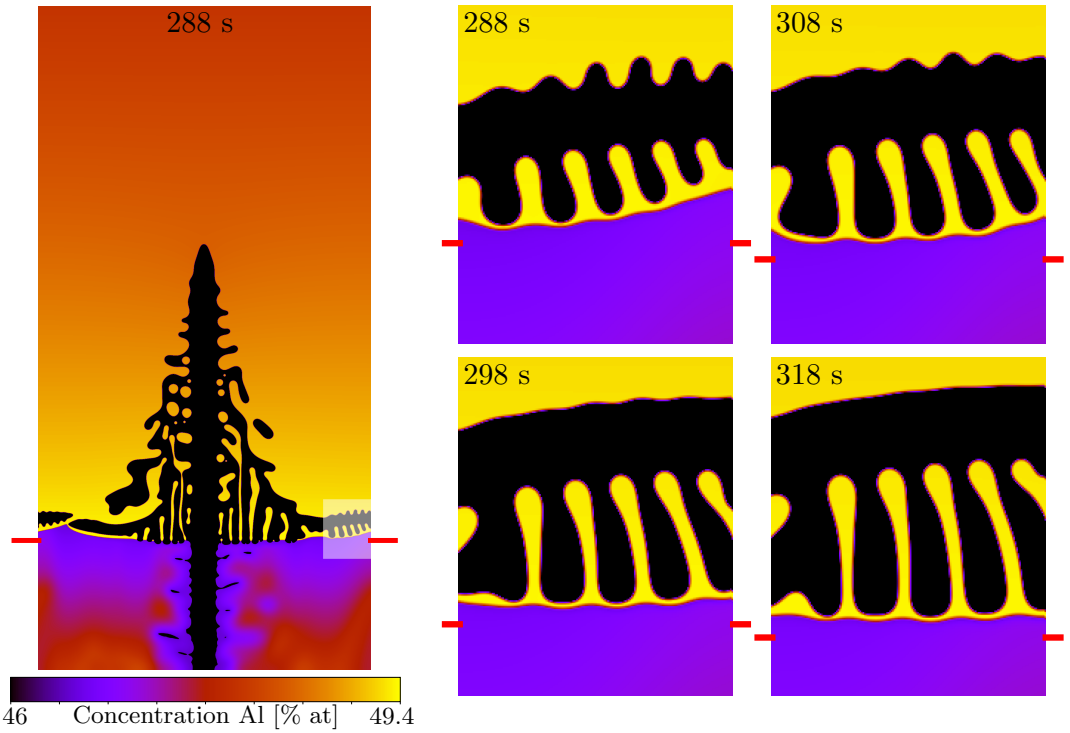

Figure 12: left : Al-concentration fields at 288 s (ΔT_{LH} in figure 7) , right : microstructure evolution at different time steps from the white dashed area on the left figure. Red markers indicate the position of the peritectic temperature (T_p).

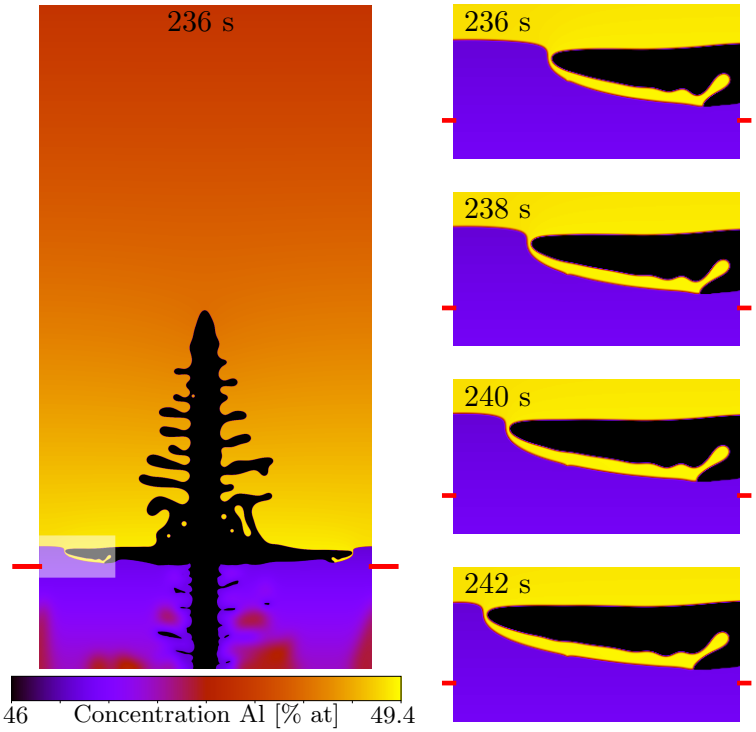

Figure 13: left : Al-concentration fields at 236 s (ΔT =10K in figure 7) , right : microstructure evolution at different time steps from the white dashed area on the left figure. Red markers indicate the position of the peritectic temperature (T_p).

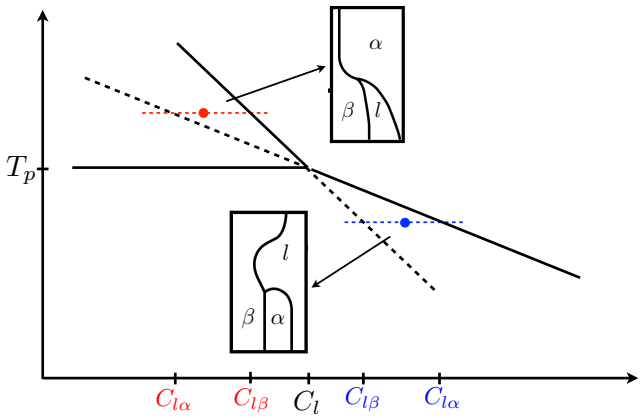

Figure 14: Close-up around the liquid concentration in the phase diagram. The liquidus lines and their metastable extensions delimitate the two-phase regions above and below T_p. The red and blue dots schematically represent, for melting above T_p and solidification below T_p respectively, the liquid concentration at the triple junction. Since the blue (red) dot lies inside (outside) the $(\alpha + L)$ two-phase region and outside (inside) the $(\beta + L)$ two-phase region, the $\alpha - L$ interface is convex (concave) and the $\beta - L$ interface is concave (convex). This is illustrated by the corresponding growth structures.

can be seen. At this time step, it is located below T_p (see the red marker in Figure 16). Liquid domains are migrating upwards in the thermal gradient according to the TGZM phenomenon. At 60s, a part of the β domain has been remelted after the migration of a liquid domain. On the other hand, while the system experiences heating (note the difference of position of T_p at 35s, 60s, 80s, 90s, 100s and 120s in the figure), the temperature of the β domain goes above T_p between 60 and 80s. Once above T_p, when a migrating liquid domain encounters the β phase, the $\alpha \rightarrow (\beta + L)$ transformation takes place rather than a simple remelting of the solidified microstructure. It is interesting to note that the newly formed fragment of β phase produced with this mechanism is larger than the β domain from which it formed: during the $\alpha \rightarrow (\beta + L)$ transformation, it grows and is then rapidly surrounded by the liquid phase (see 80s-120s). Another interesting observation, looking back into Figure 7, is that the lifetime of this fragment is rather long at the scale of the simulations. The fragment is formed between 80 and 100s and survives above 400s. In the general case where fluid flow occurs, fragments produced by this mechanism may be taken to the mush, where they could contribute to the formation of new grains in case of subsequent solidification as for example in additive manufacturing.

In their experimental study in Ti-Al alloys, Reilly *et al.* have proposed that LFM would lead to the remelting of secondary dendrite arms at the TJ to produce fragments to explain the grain refinement observed in their samples [20]. The results presented here show that the operating mechanism could be slightly different, and rather induced by the melting transformation $\alpha \rightarrow (\beta + L)$ of previously untransformed β phase. Grain refinement in peritectic alloys not containing nucleant particles has been observed since a long time in steels [36], while no explanations were given. More recently, Yasuda et al. [41] have observed refinement in the Fe-C alloy and, without proposing a precise scenario, linked it to the reverse peritectic reaction. We thus propose that the scenario relies on the LFM process. Barriobero *et al.* have shown a peritectic titanium alloy that produced fully equiaxed microstructure during additive manufacturing [37]. Additive manufacturing is a typical process involving remelting and fluid flow. The mechanism revealed in the present paper would be a plausible explanation for the grain refinement observed in all these peritectic systems.

5. Conclusion

In this paper, the microstructure evolution during solidification and partial remelting of peritectic TiAl alloys was investigated and lead to the following conclusions.

About the solidification stage, it has been shown that the diffusion around the triple junction impacts poorly the tip undercooling of the properitectic phase, and that the growth of the triple junction is mainly affected by the extent of development of the secondary dendrite arms.

A partial remelting was implemented by re-heating a solidified mushy zone to simulate what heat advection due to fluid flow could induce during a casting operation. In that case, investigating (i) the temperature difference ΔT by which the microstructure was re-heated and (ii) taking into account the latent heat, have allowed to highlight several phenomena. Close to the peritectic temperature, liquid film migration drives the microstructure evolution during the reverse peritectic transformation $\alpha \rightarrow (\beta + L)$. Diverse scenarios are evidenced depending on whether the growth takes place without triple junction from a pure α phase or with a triple junction along the α/β interface. At the scale of the mushy zone, temperature gradient zone melting also occurs but remains incomplete at the time scale investigated here. Finally, a new mechanism for fragmentation was observed: untransformed β phase, located close to the peritectic temperature and inherited from secondary dendrite arms, grow and produce fragments upon heating. The latter results can explain the propensity of peritectic alloys to exhibit finer solidification microstructures.

Acknowledgements

This work has been carried out in the framework of ESA Topical Team "Melting of Dissimilar and Multiphase Metallic alloys" under contract No. 4000123987/18.

References

References

[1] H. W. Kerr, W. Kurz, International materials reviews 41 (1996) 129–164.

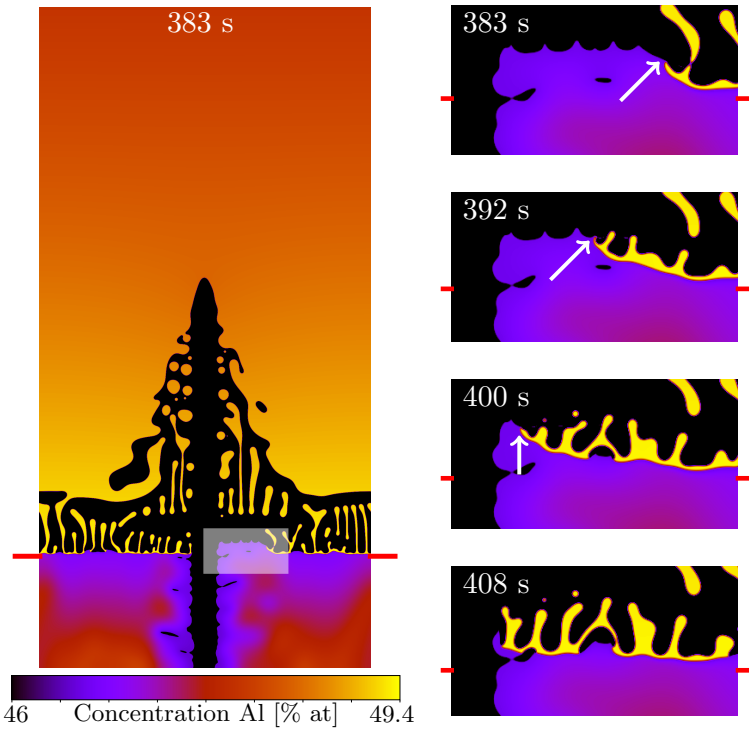

Figure 15: left : Al-concentration fields at 383 s for ΔT_{LH}, right : microstructure evolution at different time steps from the white dashed area on the left figure. Red markers indicate the position of the peritectic temperature (T_p).

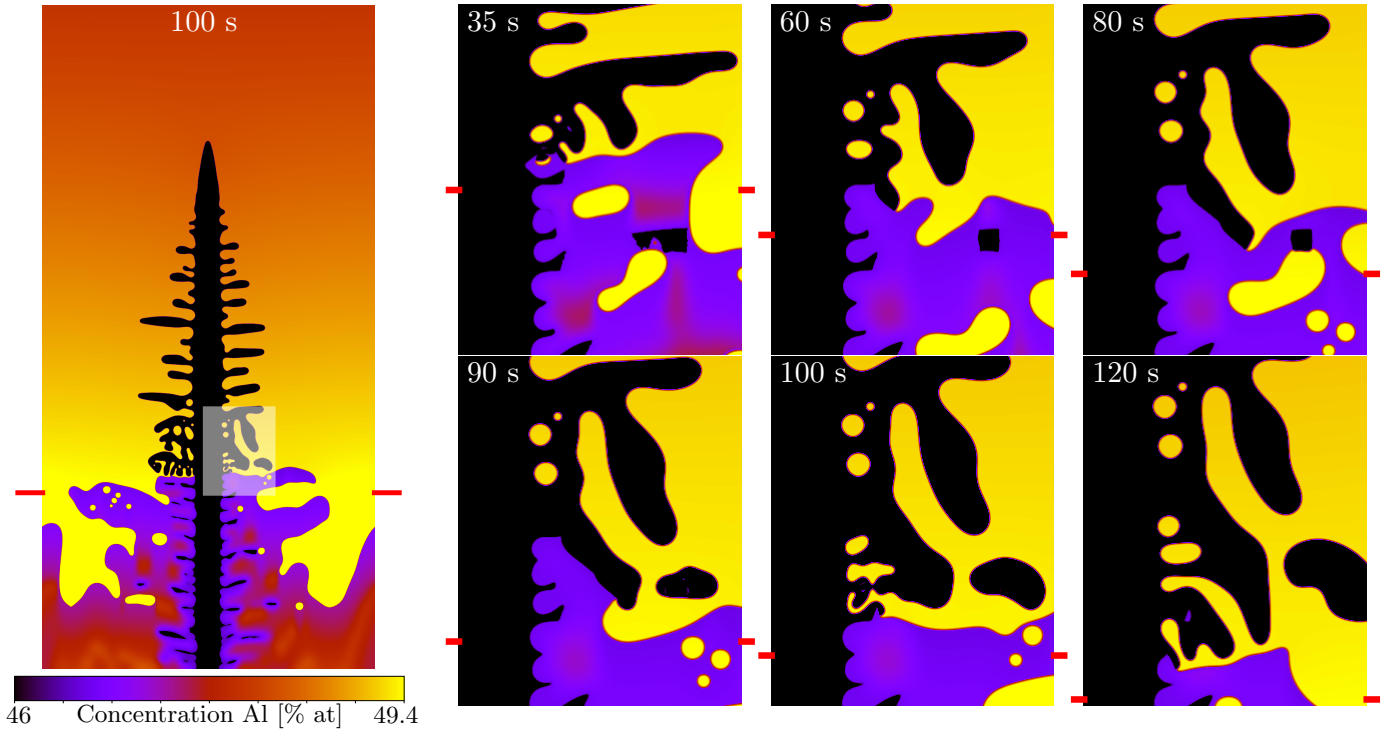

Figure 16: left : Al-concentration fields at 100 s (ΔT_{LH} in figure 7) , right : microstructure evolution at different time steps from the white dashed area on the left figure. Red markers indicate the position of the peritectic temperature (T_p)

[2] H. Fredriksson, T. Nylen, Metal Science 16 (1982) 283–294.
[3] W. Boettinger, Metal. Trans. 5 (1974) 2023–2031.
[4] J. Valloton, Phase Competition in Peritectic Cu-Sn Alloys during Solidification at Low Speed in a Diffusive Regime, Technical Report, EPFL, 2012.
[5] J. Tiaden, J. Cryst. Growth 198 (1999) 1275–1280.
[6] B. Nestler, A. Wheeler, Physica D: Nonlinear Phenomena 138 (2000) 114–133.
[7] T. Lo, S. Dobler, M. Plapp, A. Karma, W. Kurz, Acta Mater. 51 (2003) 599–611.
[8] M. Rettenmayr, International Materials Reviews 54 (2009) 1–17.
[9] T. Campanella, C. Charbon, M. Rappaz, Metal. Mater. Trans. A 35 (2004) 3201–3210.
[10] I. Cazic, J. Zollinger, S. Mathieu, M. El Kandaoui, P. Plapper, B. Appolaire, Scripta Mater. 195 (2021) 113740.
[11] N. Leriche, H. Combeau, C.-A. Gandin, M. Založnik, in: IOP Conference Series: Materials Science and Engineering, volume 84, IOP Publishing, p. 012087.
[12] H. Neumann-Heyme, K. Eckert, C. Beckermann, Physical Review E 92 (2015) 060401.
[13] T. Sato, W. Kurz, K. Ikawa, Transactions of the Japan Institute of Metals 28 (1987) 1012–1021.
[14] G. Salloum-Abou-Jaoude, G. Reinhart, H. Combeau, M. Zaloˇ znik, T. Lafford, H. Nguyen-Thi, Journal of Crystal Growth 411 (2015) 88–95. doi:10.1016/j.jcrysgro.2014.10.053.
[15] W. Tiller, Journal of Applied Physics 34 (1963) 2757–2762.
[16] G. Boussinot, M. Apel, Acta Materialia 122 (2017) 310–321. doi:10.1016/j.actamat.2016.09.053.
[17] E. Brener, D. Temkin, Acta Materialia 55 (2007) 2785–2789. doi:10.1016/j.actamat.2006.12.016.
[18] G. Boussinot, E. Brener, D. Temkin, Acta Materialia 58 (2010) 1750–1760. doi:10.1016/j.actamat.2009.11.017.
[19] C. Huang, U. Hecht, A. Bührig-Polaczek, Metal. Mater. Trans. B 51 (2020) 2252–2267.
[20] N. Reilly, B. Rouat, G. Martin, D. Daloz, J. Zollinger, Intermetallics 86 (2017) 126–133.
[21] S. Tiwari, J. Beech, Transactions of the Iron and Steel Institute of Japan 21 (1981) 554–558.
[22] B. Böttger, J. Eiken, M. Apel, Comp. Mat. Sci. 108 (2015) 282–292.
[23] J. Eiken, B. Böttger, I. Steinbach, Phys. Rev. E 73 (2006) 066122. doi:10.1103/PhysRevE.73.066122.
[24] Micress 6.4, http://www.micress.de,
[25] J. Eiken, IOP Conference Series: Materials Science and Engineering 33 (2012) 012105. doi:10.1088/1757-899X/33/1/012105.
[26] A. Carre, B. Böttger, M. Apel, J. Cryst. Growth 380 (2013) 5–13.
[27] G. Boussinot, M. Apel, U. Hecht, Materialia 11 (2020) 100744.
[28] G. Boussinot, M. Apel, Acta Mater. 122 (2017) 310–321.
[29] V. Witusiewicz, A. Bondar, U. Hecht, S. Rex, T. Velikanova, Journal of Alloys and Compounds 465 (2008) 64–77. doi:doi:10.1016/j.jallcom.2007.10.061.
[30] J. Eiken, M. Apel, V. Witusiewicz, J. Zollinger, U. Hecht, Journal of Physics: Condensed Matter 21 (2009) 464104.
[31] A. Viardin, J. Zollinger, L. Sturz, M. Apel, J. Eiken, B. R., H. U., Computational Materials Science 172 (2020) 109358. doi:doi:10.1016/j.commatsci.2019.109358.
[32] K. Kassner, C. Misbah, Phys Rev A. 44 (1991) 6513–6532. doi:10.1103/physreva.44.6513.
[33] G. Boussinot, C. Hüter, R. Spatschek, E. Brener, Acta Materialia 75 (2014) 212–218. doi:10.1016/j.actamat.2014.04.055.
[34] G. Boussinot, M. Apel, U. Hecht, Materialia 11 (2020) 100744. doi:10.1016/j.mtla.2020.100744.
[35] D. Temkin, Acta Materialia 53 (2005) 2733–2738. doi:10.1016/j.actamat.2005.02.038.
[36] P. Bibby, J. Beech, Journal of the Iron and Steel Institute 211 (1973) 290–292.
[37] P. Barriobero-Vila, J. Gussone, A. Stark, N. Schell, J. Haubrich, G. Requena, Nat. commun. 9 (2018) 1–9.
[38] Y. Song,D. Tourret,F.L. Mota, J. Pereda,B. Billia,N. Bergeon, R. Trivedi,A. Karma, Acta Materialia 150 (2018) 139–152. doi:10.1016/j.actamat.2018.03.012.
[39] H. Shibata,Y. Arai,M. Suzuki, T. Emi, Metall. Mater. Trans. B 31 5 (2000) 981–991. doi:10.1007/s11663-000-0074-3.
[40] D. Phelan,M. Reid,R. Dippenaar, Metall. Mater. Trans. A 37 3 (2006) 985–994. doi:10.1007/s11661-006-0071-5.
[41] H. Yasuda,K. Morishita,N.. Nakatsuka, T. Nishimura,M. Yoshiya,A. Sugiyama, K. Uesugi,A. Takeuchi, Nature Comm. 10 1 (2019) 3183–3183. doi:10.1038/s41467-019-11079-y.